Performance of encased granular columns considering shear-induced volumetric dilation of the fill material

Y.-S. Hong

Associate Professor, Department of Civil Engineering, Tamkang University, Tamsui, Taipei 25137, Taiwan, Telephone: +886 2 26260433, Telefax: +886 2 26209747, E-mail: yshong@mail.tku.edu.tw

Received 1 January 2012, revised 31 August 2012, accepted 3 September 2012

ABSTRACT: This numerical study investigates the behaviour of geosynthetic-encased sand columns. Based on an elastic-plastic constitutive model used with the non-associated flow rule, the prominent expansive behaviour of medium to dense sands is characterised. Numerical analysis results are verified via laboratory triaxial tests on encased sand columns, where the sand mechanical properties are extracted from simple experimental tests. The tested sand columns in the experiments consist of two sands, encased by sleeves fabricated from two geotextiles. This verification demonstrates that the sand volumetric strain profoundly affects the induced confining pressure of an encased column. Exactly how the encasement stiffness, strength and diameter of the granular column influence encased column response is also studied using numerical analyses. Numerical results indicate that the encasement induces additional confining pressure, subsequently preventing strength yield in the encased columns before the encasement reaches its yield strength. These results further demonstrate that the ratio of encasement stiffness to column diameter significantly affects the response of a granular column. Moreover, it may be unnecessary to encase a small-diameter column with a stiff encasement, whereas encasing a large diameter column with a low-stiffness encasement may produce a limited reinforcing effect.

KEYWORDS: Geosynthetics, Sand column, Numerical analysis, Encased, Triaxial compression test

REFERENCE: Hong, Y.-S. (2012). Performance of encased granular columns considering shear-induced volumetric dilation of the fill material. *Geosynthetics International*, **19**, No. 6, 438–452. [http://dx.doi.org/10.1680/gein.12.00029]

1. INTRODUCTION

Including granular material in soft soil increases the bearing capacity of a native soil. However, insufficient lateral support at a shallow column depth (i.e. in the top portion) often causes bulging failure in the top portion of the column (Hughes and Withers 1974; Hughes *et al.* 1975; Madhav and Miura 1994; Gniel and Bouazza 2009). There is a practice to increase the bearing capacity of a granular column by reinforcing the column with a tensile resistant material. Previous studies have demonstrated the feasibility of encapsulating all or a portion of the column with geosynthetics as an adaptable reinforcement practice (Kempfert *et al.* 1997; Raithel and Kempfert 2000; Alexiew *et al.* 2005; Raithel *et al.* 2005; Madhavi and Murthy 2007; de Mello *et al.* 2008; Sivakumar Babu *et al.* 2008; Araujo *et al.* 2009; Yoo 2010).

The many elements affecting the bearing capacity of a reinforced column embedded in soft soil include the granular and reinforcing materials, the surrounding soft soil, the interfacial characteristics of the various materials and the geometric and mechanical boundary conditions. The load–settlement behaviour of reinforced columns in single or grouped formation has received considerable attention. These studies include theoretical and numerical analyses, laboratory experimental investigations and field applications. Additionally, on the basis of results of triaxial tests (e.g. axial stress–strain–volumetric strain), the effectiveness of a reinforced column has been analysed (e.g., increases in strength and stiffness and expansion restraint) or the feasibility of numerical or theoretical methods has been validated (Broms 1977; Gray and Al-Refai 1986; Chandrasekaran *et al.* 1989; Rajagopal *et al.* 1999; Raithel and Kempfert 2000; Kempfert 2003; Murugesan and Rajagopal 2006; Malarvizhi and Ilamparuthi 2007; Wu and Hong 2009; Wu *et al.* 2009; Yoo and Kim 2009; Khabbazian *et al.* 2010; Yoo 2010; Zhang *et al.* 2011). Moreover, single or grouped column behaviour embedded in soft soil was studied using model tests (Ayadat and Hanna 2005; Murugesan and Rajagopal 2007, 2010; Gniel and Bouazza 2009; Ali *et al.* 2012). The effectiveness of reinforced column practices in the field was also described (Broms 1995; Alamgir *et al.* 1996;

Nods 2002; Raithel *et al.* 2002; Araujo *et al.* 2009). These studies found that encasement significantly improves the bearing capability and lateral constraint of a granular column.

The increase in axial strain causes lateral column expansion and compression of the surrounding soft soil, subsequently causing circumferential stress from the encasement; meanwhile, compression of the surrounding soil induces additional earth pressure to act on the column. The reinforced column in the field is thus subjected to increasing axial stress while, coincidentally, the confining pressure is increased. These problems can be solved in theoretical and numerical analyses by modelling the mechanical properties of the material as a function of the monotonically increasing confining pressure.

The numerical method has advantages over the theoretical method in analysing structures with complex geometric and load conditions such as columns embedded in limited radial spacing with non-uniform pressure distributed along the column length. By using a representative single column and its influential boundary, a 'unit cell' concept is introduced to the numerical method for group column analysis (Shahu *et al.* 2000; Han and Gabr 2002; Ambily and Gandhi 2007; Yoo and Kim 2009; Lo *et al.* 2010; Pulko *et al.* 2011). A stone-column reinforced foundation was also analysed using a homogenisation technique (Canetta and Nova 1989; Lee and Pande 1998).

Variations in the confining pressure during column axial loading should be expressed explicitly since confining pressure significantly affects the mechanical properties of a granular material. The confining pressure of an encased column depends strongly on the volumetric behaviour of a column because volumetric strain induces column expansion and radial strain, subsequently increasing the circumferential stress in the encapsulating reinforcement and cavity pressure offered by the surrounding soft soil. A numerical model capable of accurately evaluating volumetric strain is thus essential to analyse the bahaviour of reinforced granular columns, single or grouped, while embedded in soft soil.

This study elucidates the behaviour of an encased granular column using a numerical method. The proposed method incorporates the elastic-plastic constitutive law with the non-associated flow rule for filled material and the elastic-perfectly plastic relationship for encasement. In a numerical analysis the prediction accuracy and target system parameter availability are important concerns (Huang *et al.* 2009). The proposed model is based on the above concerns and the fact that the material mechanical parameters are extracted from simple tests, e.g., triaxial compression test for pure sand and load–elongation tests for reinforcement. The proposed method is validated through laboratory experimental triaxial tests on un-reinforced and encased sand columns. With its easily accessed parameters, the proposed method provides a highly effective means of analysing reinforced columns embedded in the field, which may encounter complex circumstances. In addition, a series of parametric studies thoroughly elucidates the influential factors for an encased column.

2. NUMERICAL MODELING

2.1. Soil elastic-plastic model

This study develops a model based on the theory of non-associated plasticity flow rules to elucidate the constitutive behaviour of the sand filled in the column. The required parameters in the analyses include the elastic modulus, bulk modulus, yield function and plastic potential function, as derived from triaxial compression tests for a cylindrical sand column specimen. The following subsections describe the mobilised friction angle and mobilised dilatancy angle concepts used in this analysis.

2.1.1. *Mobilised friction angle*

To more accurately represent the continuous strain-hardening behaviour of sand, a yield function f controlled by the mobilised friction angle can be expressed as

$$f = \sigma_1 - \sigma_3 N_{\phi^*} - 2c\sqrt{N_{\phi^*}} \tag{1}$$

where $N_{\phi^*} = (1 + \sin\phi^*)/(1 - \sin\phi^*)$; $\phi^* =$ mobilised friction angle of the soil; $c =$ cohesion of the soil; and σ_1, $\sigma_3 =$ major and minor principal stresses.

For a cohesionless soil ($c = 0$), the mobilised friction angle is defined by the principal stresses as

$$\phi^* = \sin^{-1}\left(\frac{\sigma_1 - \sigma_3}{\sigma_1 + \sigma_3}\right) \tag{2}$$

The mobilised friction angle generally varies with the principal stress values σ_1 and σ_3 (Equation 2). If stresses σ_1 and σ_3 produce the yield state of a material, the yield stresses also induce accumulated shear plastic strain ε_s^p in a material. Therefore, the mobilised friction angle ϕ^* can be correlated with the accumulated shear plastic strain ε_s^p.

For a cylindrical specimen subjected to triaxial compression stresses, the accumulated shear plastic strain is defined as (Miura and Toki 1982)

$$\varepsilon_s^p = \frac{2}{3}(\varepsilon_a^p - \varepsilon_r^p) = \varepsilon_a^p - \frac{1}{3}\varepsilon_v^p \tag{3}$$

where $\varepsilon_a^p =$ accumulated axial plastic strain; $\varepsilon_r^p =$ accumulated radial plastic strain; and $\varepsilon_v^p =$ accumulated volumetric plastic strain.

In the elastic-plastic model, the accumulated shear plastic strain can be expressed as

$$\begin{aligned}\varepsilon_s^p &= \varepsilon_a - \varepsilon_a^e - \frac{1}{3}\left(\varepsilon_v - \varepsilon_v^e\right)\\ &= \left(\varepsilon_a - \frac{1}{3}\varepsilon_v\right) - \Delta\sigma\left(\frac{1}{E} - \frac{1}{9B}\right)\end{aligned} \tag{4}$$

where $\varepsilon_a =$ axial strain; $\varepsilon_a^e =$ axial elastic strain; $\varepsilon_v =$ volumetric strain; $\varepsilon_v^e =$ volumetric elastic strain; $\Delta\sigma =$ deviatoric stress $= \sigma_1 - \sigma_3$; $E =$ elastic modulus; and $B =$ bulk modulus.

Equation 4 reveals that the accumulated shear plastic strain can be obtained from the known deviatoric stress and the measured axial and volumetric strains. Correspondingly, the relationship between the accumulated shear plastic strain and mobilised friction angle can be established using values obtained from Equations 2 and 4.

2.1.2. *Mobilised dilatancy angle*

The direction of plastic strain increment is not perpendicular to the yield surface since some energy loss occurs during shearing. Therefore, a plastic potential function g is necessary to describe the plastic strain increment (referred to as the non-associated flow rule). The plastic potential function g for a non-associated flow rule can be expressed as

$$g = \sigma_1 - \sigma_3 N_{\psi^*} - 2c\sqrt{N_{\psi^*}} \tag{5}$$

where g = plastic potential function; $N_{\psi^*} = (1+\sin\psi^*)/(1-\sin\psi^*)$; and ψ^* = mobilised dilatancy angle.

According to the flow rule, the plastic strain increment $d\varepsilon_{ij}^{p}$ is defined as

$$d\varepsilon_{ij}^{p} = \lambda \frac{\partial g}{\partial \boldsymbol{\sigma}_{ij}} \tag{6}$$

where $d\varepsilon_{ij}^{p}$ = plastic strain increment; λ = a positive scale value; and $\boldsymbol{\sigma}_{ij}$ = stress tensor.

The volumetric plastic strain increment $d\varepsilon_{v}^{p}$ denotes the summation of plastic strain increments in three principal directions, which can be written as

$$d\varepsilon_{v}^{p} = d\varepsilon_{1}^{p} + 2d\varepsilon_{3}^{p} = \lambda(1 - N_{\psi^*}) \tag{7}$$

where $d\varepsilon_{1}^{p}$ = plastic strain increment in the axial direction = λ; and $d\varepsilon_{3}^{p}$ = plastic strain increment in the radial directions.

By substituting $N_{\psi^*} = (1+\sin\psi^*)/(1-\sin\psi^*)$ into Equation 7 and rearranging the terms, the mobilised dilatancy angle ψ^* can be written as

$$\frac{d\varepsilon_{v}^{p}}{d\varepsilon_{1}^{p}} = \left(1 - \frac{1+\sin\psi^*}{1-\sin\psi^*}\right) = \left(\frac{-2\sin\psi^*}{1-\sin\psi^*}\right) \tag{8}$$

or

$$\psi^* = \sin^{-1}\left(\frac{d\varepsilon_{v}^{p}}{d\varepsilon_{v}^{p} - 2d\varepsilon_{1}^{p}}\right) \tag{9}$$

The measured volumetric and axial strains and the deviatoric stress accomplish the calculation of Equation 9.

2.2. Sand properties and parameters for numerical modelling

This study also develops numerical expressions specifying the constitutive behaviour of the test sands as a function of monotonically increased confining pressure. The strain hardening constitutive model following the non-associated flow rule characterises the prominent expansive behaviour of the medium to dense sands. Next, the mechanical properties for numerical analysis are extracted based on the experimental results obtained from cylindrical sand specimens subjected to triaxial compression conditions. Because no significant residual strength is observed, the sand specimen is assumed to have no softening behaviour. This section introduces the acquisition procedures in determining the material parameters for the numerical formations.

2.2.1. *Modulus of elasticity of the test sands*

One of the two sands, sub-angular and round-grained shapes (designated as S1 and S2), and one of two geotextile sleeves (designated as GT1 and GT2) constitute the encased sand column. The sub-angular sand S1 has a specific gravity of $G_s = 2.63$, maximum dry unit weight of $\gamma_{d\max} = 16.48$ kN/m^3, and minimum dry unit weight of $\gamma_{d\min} = 13.73$ kN/m^3. The round-shaped sand S2 has a specific gravity of $G_s = 2.65$, maximum dry unit weight of $\gamma_{d\max} = 17.56$ kN/m^3, and minimum dry unit weight of $\gamma_{d\min} = 14.62$ kN/m^3. Gradations of the sands are as follows. S1: $D_{10} = 0.70$ mm, $D_{30} = 0.76$ mm, $D_{50} =$ 0.84 mm, $D_{60} = 0.92$ mm; coefficient of uniformity equal to 1.31; coefficient of gradation equal to 0.90. S2: $D_{10} = 0.24$ mm, $D_{30} = 0.37$ mm, $D_{50} = 0.40$ mm, $D_{60} =$ 0.41 mm; coefficient of uniformity equal to 1.71; coefficient of gradation equal to 1.39. Both sands are classified as poorly graded sand (SP) according to the Unified Soil Classification System. Triaxial compression tests are conducted on each type of dry sand compacted to 60% relative density. Wu and Hong (2009) describe in detail triaxial compression tests on unreinforced and encased columns.

Figure 1 displays the axial stress–strain–volumetric strain relation for cylindrical sand specimens subjected to various chamber pressures. Notably, the initial tangential modulus of the deviatoric stress–strain curve is taken as the elastic modulus of the sand since sand behaves elastically only in the minimal axial strain range. The solid lines in Figure 1 denote the numerical analysis results using the current model parameters. Figure 2 shows the relationship between the elastic modulus and chamber pressure for the test sands. Regression expressions for parameter E are developed from test results and expressed as

$$E(\text{kPa}) = \left[4.702\log\left(\frac{\sigma_3}{P_a}\right) + 4.533\right] \times 10^4 \quad \text{for } \sigma_3 \geqslant 20 \text{ kPa and sand S1} \tag{10}$$

and

$$E(\text{kPa}) = 261.683\sigma_3 + 24330.2 \quad \text{for } \sigma_3 \geqslant 20 \text{ kPa and sand S2} \tag{11}$$

where $P_a = 1$ kg/cm^2 = 101.4 kPa.

The two regression functions are formulated using triaxial compression test results conducted over the confining pressure ranges of 20–500 kPa, and 20–200 kPa for soils S1 and S2, respectively. The Poisson ratio of the sands is taken as 0.35, and the bulk moduli are calculated accordingly.

2.2.2. *Mobilised friction angles of the test sands*

In the continuous strain-hardening model, subjection of the soil specimen to principal yield stresses σ_1 and σ_3 induces mobilised friction angle ϕ^* (Equation 2) and

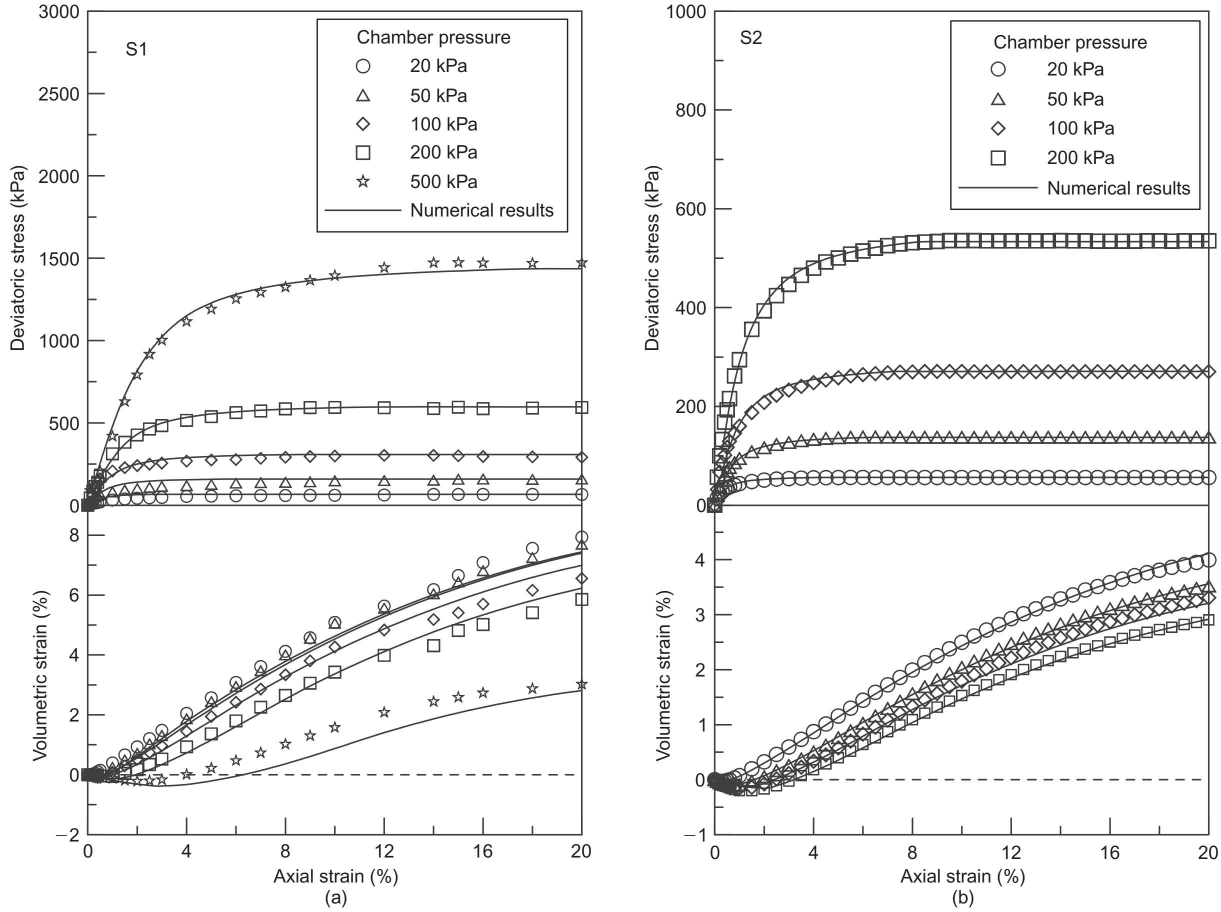

Figure 1. Triaxial compression test results for the pure sands: (a) S1; (b) S2

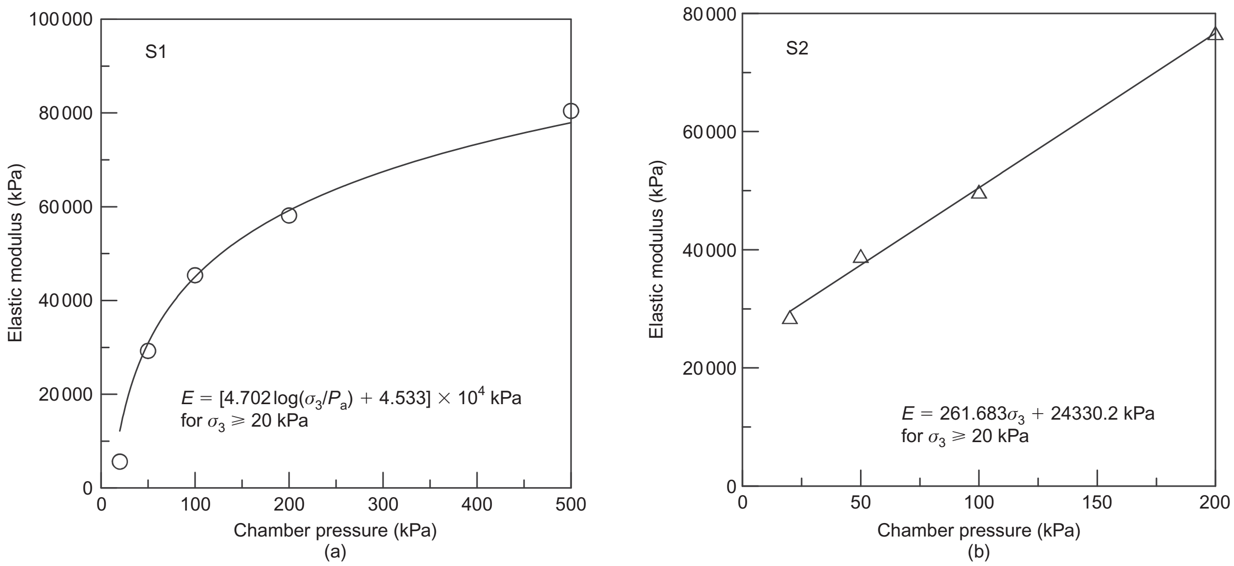

Figure 2. Elastic modulus against chamber pressure for the test sands: (a) S1; (b) S2

accumulated shear plastic strain ε_s^p (Equation 4). Figure 3 plots the relations between these two parameters for the two test sands. This figure reveals that mobilised friction angle increases with increasing accumulated shear plastic strain and reaches a peak and persistent value. The peak accumulated shear plastic strain and the peak deviatoric stress occur simultaneously. The accumulated shear plastic strain at the peak deviatoric stress depends on the confining pressure. Figure 4 shows the relationship between the accumulated shear plastic strain at the peak deviatoric stress $\varepsilon_{s,peak}^p$ and the confining pressure. The relation can be expressed as

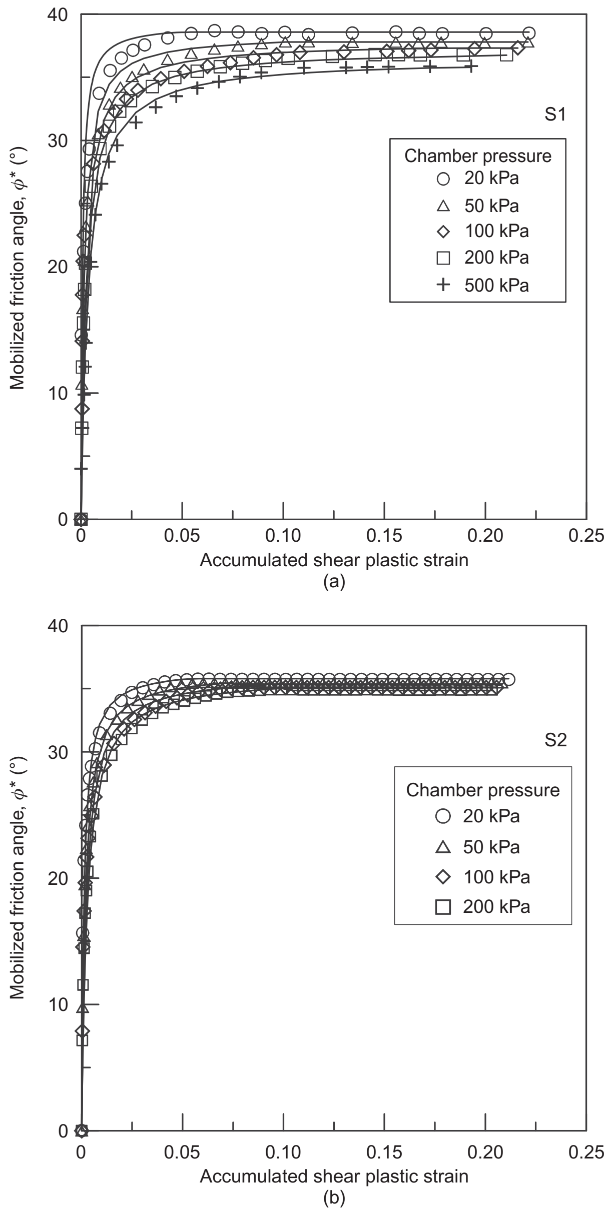

Figure 3. Mobilised friction angle against accumulated shear plastic strain for the test sands: (a) S1; (b) S2

$$\varepsilon^{\mathrm{p}}_{\mathrm{s,peak}} = 0.047\ln(\sigma_3) - 0.094 \quad \text{for sand S1} \tag{12}$$

and

$$\varepsilon^{\mathrm{p}}_{\mathrm{s,peak}} = 0.016\ln(\sigma_3) + 0.013 \quad \text{for sand S2} \tag{13}$$

where $\varepsilon^{\mathrm{p}}_{\mathrm{s,peak}}$ = accumulated shear plastic strain at peak deviatoric stress.

For easy numerical expressions, each curve in Figure 3 is divided into two segments, pre-peak and post-peak segments. In the pre-peak stress segment, the relationship between the mobilised friction angle ϕ^* and the accumulated shear plastic strain $\varepsilon^{\mathrm{p}}_{\mathrm{s}}$ is delineated using a parabolic function. The mobilised friction angle in the post-peak stress segment has a constant value and depends only on the confining pressure. The relationships between the mobilised friction angle and the accumulated shear plastic strain for the test sands (Figure 3) are regressed and expressed as

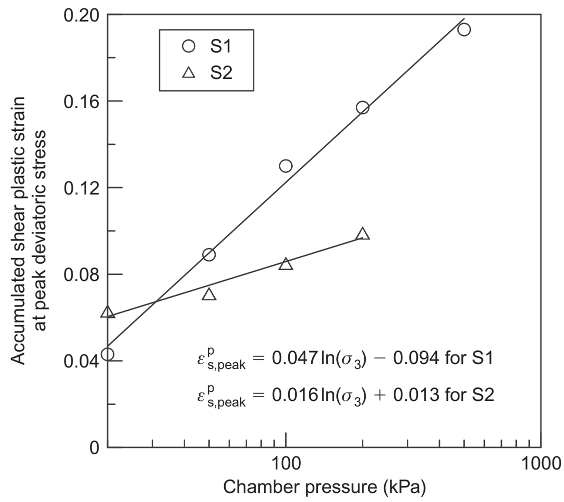

Figure 4. Accumulated shear plastic strain at peak stress against chamber pressure for the test sands

$$\begin{aligned}\phi^* &= [1 - u(\varepsilon^{\mathrm{p}}_{\mathrm{s}} - \varepsilon^{\mathrm{p}}_{\mathrm{s,peak}})] \\ &\quad \times \left\{ \frac{10000\varepsilon^{\mathrm{p}}_{\mathrm{s}}}{[0.248\ln(\sigma_3) - 0.557] + [5.805\ln(\sigma_3) + 238]\varepsilon^{\mathrm{p}}_{\mathrm{s}}} \right\} \\ &\quad + u(\varepsilon^{\mathrm{p}}_{\mathrm{s}} - \varepsilon^{\mathrm{p}}_{\mathrm{s,peak}})[(-0.735)\ln(\sigma_3) + 40.695]\end{aligned} \tag{14}$$

for sand S1, and

$$\begin{aligned}\phi^* &= [1 - u(\varepsilon^{\mathrm{p}}_{\mathrm{s}} - \varepsilon^{\mathrm{p}}_{\mathrm{s,peak}})] \\ &\quad \times \left\{ \frac{10000\ \varepsilon^{\mathrm{p}}_{\mathrm{s}}}{[0.198\ln(\sigma_3) - 0.262] + [1.878\ln(\sigma_3) + 268]\varepsilon^{\mathrm{p}}_{\mathrm{s}}} \right\} \\ &\quad + u(\varepsilon^{\mathrm{p}}_{\mathrm{s}} - \varepsilon^{\mathrm{p}}_{\mathrm{s,peak}})[(-0.368)\ln(\sigma_3) + 36.797]\end{aligned} \tag{15}$$

for sand S2, where u = the unit step function.

Figure 3 summarises the results of these two regression functions (Equations 14 and 15), which correlate well with the experimental results.

2.2.3. *Mobilised dilatancy angles of the test sands*

Triaxial compression test results indicate that a sand column specimen contracts and then expands with an increasing axial strain. The axial compression and volumetric contraction or expansion cumulatively induce lateral expansion in the column. This lateral deformation stretches the sleeve, subsequently leading to circumferential tensile stress (i.e. hoop stress) in an encased column. A numerical scheme must be developed, capable of modelling the volumetric behaviour of the constituent sand in a column to vary the confining pressure acting on the encased column during axial compression.

Most numerical analyses on encased column behaviour model sand as an elastic-perfectly plastic model with Mohr–Coulomb yield criteria due to its simplicity. However, this model deduces that soil contracts until stress yield occurs, thus contradicting the nature of medium to dense sand and ultimately underestimating both the volume expansion of medium to dense sand and the reinforcing effect of an encasing sleeve. Therefore, this study more thoroughly elucidates the soil behaviour by devising more complex procedures than the elastic-perfectly plastic model with a simple yield criterion.

The expansive behaviour of a granular material can be delineated through the change in dilatancy angle. According to subsection 2.1.2. the dilatancy angle of a granular material is expressed as a function of the volumetric and axial strain increments (Equation 9), whereas these two strain increments are related to the accumulated shear plastic strain. Based on the experimental results, Figure 5 shows the relation between the mobilised dilatancy angle and the accumulated shear plastic strain for the test sands.

The data in Figure 5 are grouped into three segments for ease of numerical expression. The two neighbouring segments are divided on the basis of the stages of volumetric strain: contraction, expansion and residual stages. Exactly how the mobilised dilatancy angle and the accumulated shear plastic strain are related is described using a function. The three stages are as follows.

(*a*) Contraction stage, in which no dilatancy angle occurs ($\psi^* = 0$) in the sand behaviour (i.e. $\varepsilon_s^p \leqslant \varepsilon_{s,exp}^p$) (Figure 5). Therefore, the mobilised dilatancy angle in this stage is assumed to be zero. Figure 1 reveals that the axial strains corresponding to the initiation of expansive and residual stages in the test sands depend on the confining pressure. A higher confining pressure extends both the contraction and expansion behaviours of a column to greater axial strains. Figure 6 illustrates that the accumulated shear plastic strain at initial dilation and the confining pressure are related. These two variables are regressed using Equations 16–19.

For sand S1,

$$\varepsilon_{s,exp}^p = 0 \quad \text{for } \sigma_3 < 39\,\text{kPa} \tag{16}$$

and

$$\varepsilon_{s,exp}^p = \frac{(0.329\sigma_3 - 12.578)}{10\,000} \quad \text{for } \sigma_3 \geqslant 39\text{ kPa} \tag{17}$$

and for sand S2,

$$\varepsilon_{s,exp}^p = 0 \quad \text{for } \sigma_3 < 11\,\text{kPa} \tag{18}$$

and

$$\varepsilon_{s,exp}^p = 0.005\ln(\sigma_3) - 0.012 \quad \text{for } \sigma_3 \geqslant 11\,\text{kPa} \tag{19}$$

where $\varepsilon_{s,exp}^p$ = accumulated shear plastic strain at initial dilation.

(*b*) Expansion stage, in which the dilatancy angle is developed and increased with the increase in axial strain up to a peak value (i.e. $\varepsilon_{s,exp}^p < \varepsilon_s^p \leqslant \varepsilon_{s,res}^p$). The mobilised dilatancy angle and the accumulated

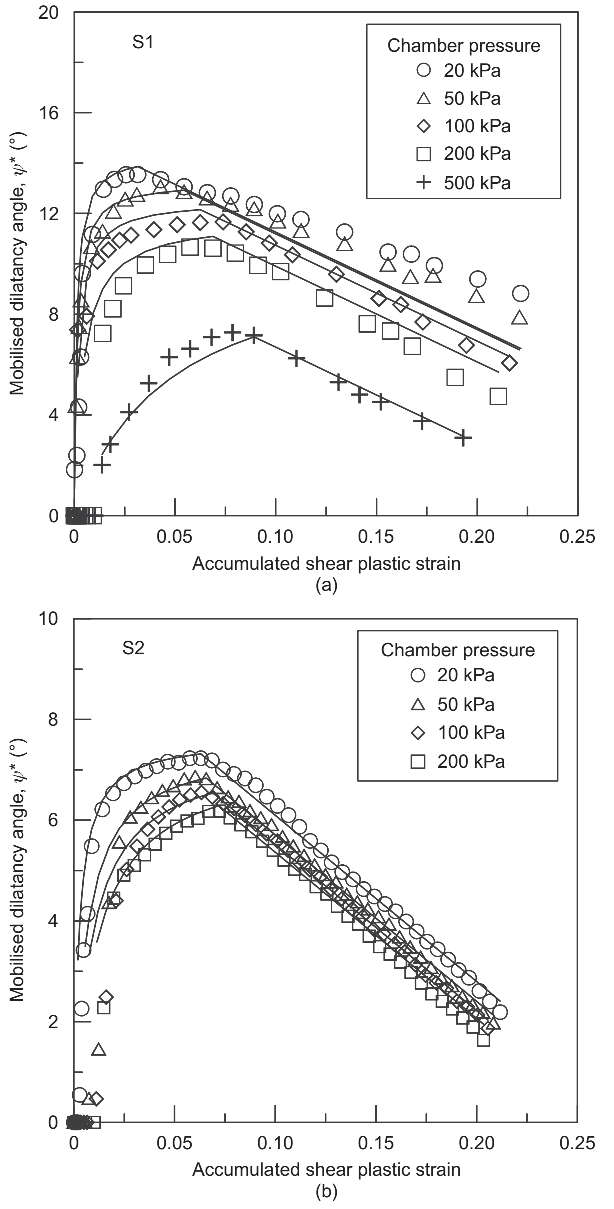

Figure 5. Mobilised dilatancy angle against accumulated shear plastic strain for the test sands: (a) S1 (b) S2

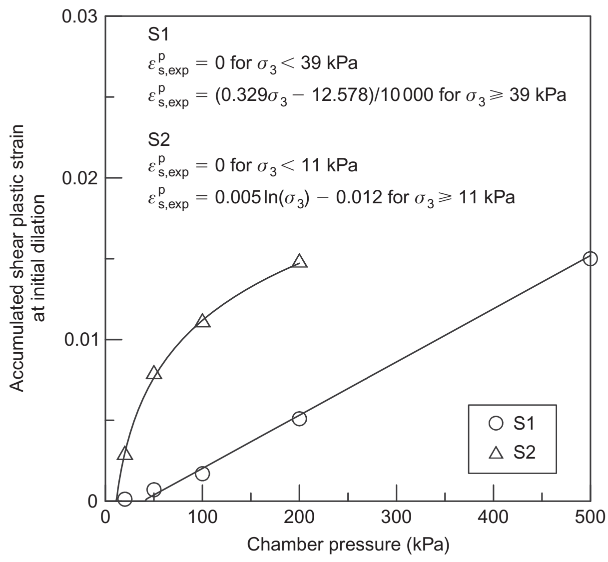

Figure 6. Accumulated shear plastic strain at initial dilation against chamber pressure for the test sands

shear plastic strain are related using a hyperbolic function.

Figure 7 shows how the accumulated shear plastic strain at the initial residual stage and the confining pressure are related. These two variables are regressed using Equations 20 and 21.
For sand S1,

$$\varepsilon^{p}_{s,res} = 0.017\ln(\sigma_3) - 0.018 \tag{20}$$

and for sand S2,

$$\varepsilon^{p}_{s,res} = 0.004\ln(\sigma_3) + 0.051 \tag{21}$$

where $\varepsilon^{p}_{s,res}$ = accumulated shear plastic strain at the peak mobilised dilatancy angle, or the initial residual stage.

(*c*) Residual stage, in which the post peak value in the mobilised dilatancy angle decreases with an increasing accumulated shear plastic strain (i.e. $\varepsilon^{p}_{s} > \varepsilon^{p}_{s,res}$). The decreasing rate is irrelevant to the confining pressure value. Exactly how these two parameters are related is modelled as a decreasing linear function. The data shown in Figure 5 are regressed using Equations 22 and 23.

For sand S1,

$$\psi^{*} = u(\varepsilon^{p}_{s} - \varepsilon^{p}_{s,exp})u(\varepsilon^{p}_{s,res} - \varepsilon^{p}_{s})\left[f^{*}(\varepsilon^{p}_{s})\right] + u(\varepsilon^{p}_{s} - \varepsilon^{p}_{s,res})\left[f^{*}(\varepsilon^{p}_{s,res}) - 38(\varepsilon^{p}_{s} - \varepsilon^{p}_{s,res})\right] \tag{22}$$

where

$$f^{*}(\varepsilon^{p}_{s}) = \frac{\varepsilon^{p}_{s}}{e^{(0.008\sigma_3 - 9.546)} + [0.007\ln(\sigma_3) + 0.046]\varepsilon^{p}_{s}}$$

and for sand S2,

$$\psi^{*} = u(\varepsilon^{p}_{s} - \varepsilon^{p}_{s,exp})u(\varepsilon^{p}_{s,res} - \varepsilon^{p}_{s})\left[f^{*}(\varepsilon^{p}_{s})\right] + u(\varepsilon^{p}_{s} - \varepsilon^{p}_{s,res})\left[f^{*}(\varepsilon^{p}_{s,res}) - 33(\varepsilon^{p}_{s} - \varepsilon^{p}_{s,res})\right] \tag{23}$$

where

$$f^{*}(\varepsilon^{p}_{s}) = \frac{10\,000\,\varepsilon^{p}_{s}}{[5.525\ln(\sigma_3) - 12.948] + [23.469\ln(\sigma_3) + 1239.466]\varepsilon^{p}_{s}}$$

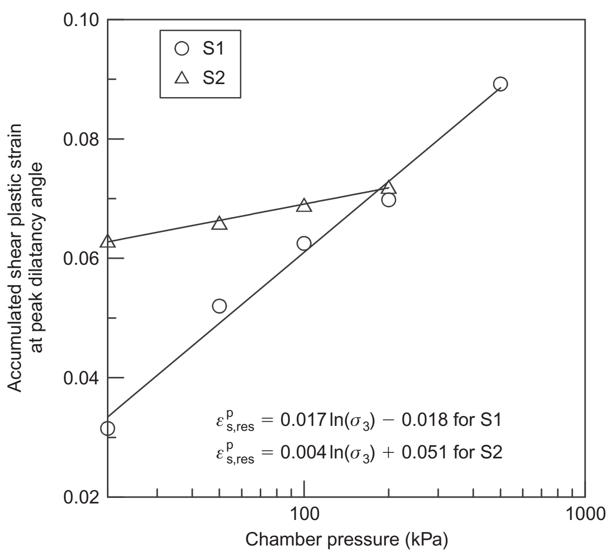

Figure 7. Accumulated shear plastic strain at peak dilatancy angle against chamber pressure for the test sands

Figure 5 reveals that a sand specimen subjected to a higher confining pressure reaches its peak dilatancy angle at a greater plastic shear strain. The regression equations (Equations 22 and 23) produce the solid lines in Figure 5, where the mobilised dilatancy angle varies with the accumulated shear plastic strain in three fractions. The results evaluated using the numerical functions (Equations 22 and 23) correlate well with those from the experimental tests, especially for sand S2, whereas the round shaped sand dilates less and the specimens are tested under a narrower chamber pressure range (20–200 kPa).

2.3. Encasement property parameters for numerical modelling

2.3.1. *Constitutive properties of the encasement*

By using the tensile load–strain relation obtained from the wide-width test, the reinforcement properties are derived on the basis of the results depicted in Figure 8. To incorporate the effect of sewing on the extension behaviour of the sleeve in the triaxial compression test, two pieces of geotextile were sewn into a 200 mm × 100 mm test specimen. The tensile test was performed using a strain rate of 0.24 mm/min. This rate is markedly slower than that used in the ASTM specification (10 mm/min) but approximates the circumferential strain rate of the geotextile sleeves in the triaxial tests.

In the experimental tests for encased columns, the maximum circumferential strain of the reinforcement is approximately 13–15% corresponding to 20% axial column strain, depending on the filled sand and chamber pressure. In this strain range, the test geotextiles (GT1 and GT2) exhibit a nearly linear tensile load–strain relationship. The reinforcement is thus modelled as a linear elastic-perfectly plastic material. One third of the peak strength secant modulus is assumed here to represent the elastic modulus. Given that this experimental test does not address a situation in which the encased column encounters encasement failure, the high rupture strain of the geotextiles used can avoid tensile failure of the encasement. In the real-case problem, the use of high-tensile rupture encasement may be unnecessary.

2.3.2. *Poisson ratio of the encasement*

For an encased column with initial and deformed radii of r_0 and r_1, the encasement circumferential strain equals the radial strain of a column as

$$\varepsilon_{\theta} = \frac{2\pi(r_1 - r_0)}{2\pi r_0} = \frac{r_1 - r_0}{r_0} = \varepsilon_{rad} \tag{24}$$

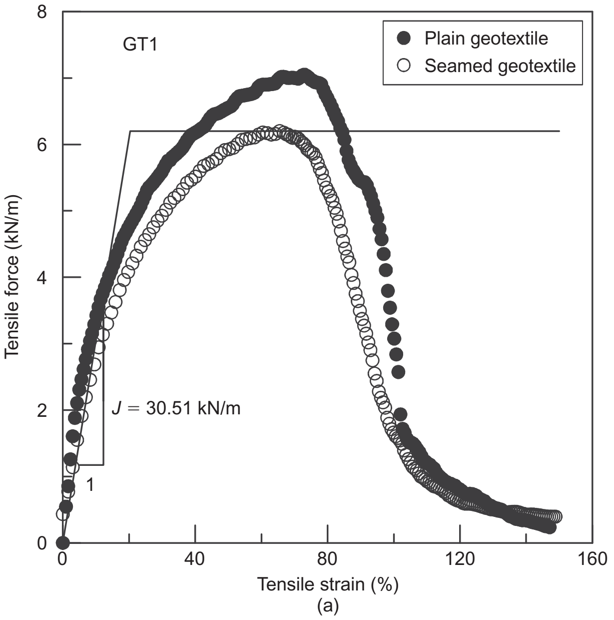

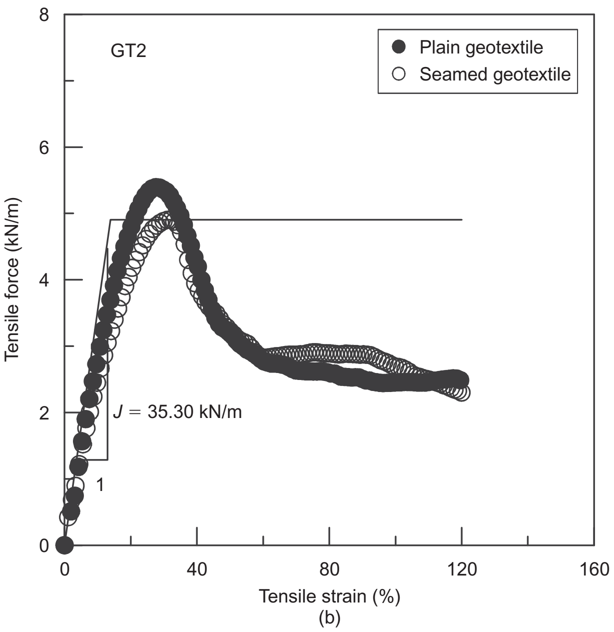

Figure 8. The tensile force–strain relations for the test geotextiles: (a) GT1 (b) GT2

where ε_θ, ε_{rad} = the encasement circumferential strain and radial strain of column.

If a flexible material such as a geosynthetic is used to encase the granular column, the encased column axial compression does not induce circumferential tensile strain in the encasement through Poisson's effect because the encasement only resists tension. The sleeve wrinkles when the axial load is applied to the encased column. Additionally, the circumferential tensile strain (as derived in Equation 24) is smaller than the axial compressive strain, explaining why circumferential tensile strain caused by column expansion does not induce axial strain through Poisson's effect. Therefore, the Poisson ratio of the encasement is taken as zero in the analysis.

2.4. Outline of the analysis

The behaviour of the encased sand columns is analysed using the constitutive properties of the constituents described in subsections 2.2. and 2.3. Figure 9 displays a symmetrical model of a 70 mm × 140 mm (diameter × length) cylindrical sand column specimen encased in a geotextile sleeve. The numerical analysis is performed using the commercial code FLAC. The encased column, subjected to a constant chamber pressure, is compressed in the axial direction by applying a 10^{-9} m/step rate on the upper boundary. Because the encasement and the soil deform simultaneously in the axial direction, no interfacial element is applied to the interface of these materials.

3. NUMERICAL RESULTS

3.1. Validation of the proposed model

The triaxial compression test results calculated using the proposed method for pure sands are presented as solid lines in Figure 1. At a certain axial strain, the maximum discrepancy in deviatoric stresses between the measured and numerically calculated values is less than 3%. However, the measured and numerically calculated volumetric strains have a greater discrepancy between each other. The sub-angular sand S1 produces a higher volumetric strain

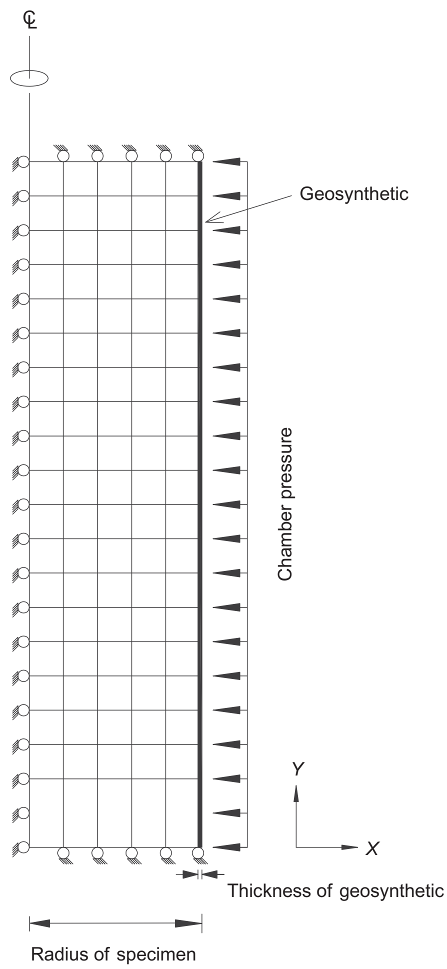

Figure 9. The element mesh for numerical analysis

than the round-shaped sand S2; in addition, the maximum discrepancy between the calculated and measured volumetric strain at 20% axial strain for the sand S1 is 7%.

Figure 10 shows numerical calculations using an elastic-perfectly plastic model with Mohr–Coulomb yield criteria. This figure reveals that this model with a hyperbolic stress–strain function can accurately predict the deviatoric stress–strain relation. Nevertheless, large discrepancies arise between the calculated and measured volumetric strains because the model infers contractive behaviour in the material until yielding.

Comparing the experimental and numerical results for an encased sand column demonstrates the advantages of mobilised friction and dilatancy angle modelling in this study. Figure 11 displays the deviatoric stress and volumetric strain against axial strain for a 70 mm diameter S2 sand column encased in a GT2 geotextile under 50 kPa chamber pressure. The proposed model accurately predicts both deviatoric stress and volumetric strain, whereas predictions using an elastic-perfectly plastic model deviate strongly from the measured values owing to improper volumetric predictions. The simple model underestimates the deviatoric stress owing to its inability to elucidate the expansive behaviour of a granular material in the early strained stage.

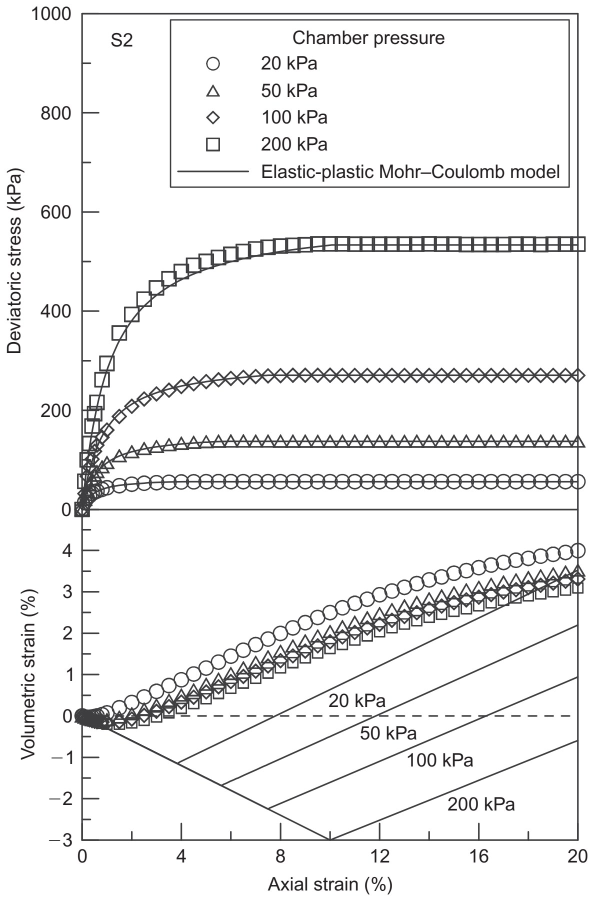

Figure 10. The numerically calculated results for a cylindrical sand column using simple elastic-plastic Mohr–Coulomb criterion

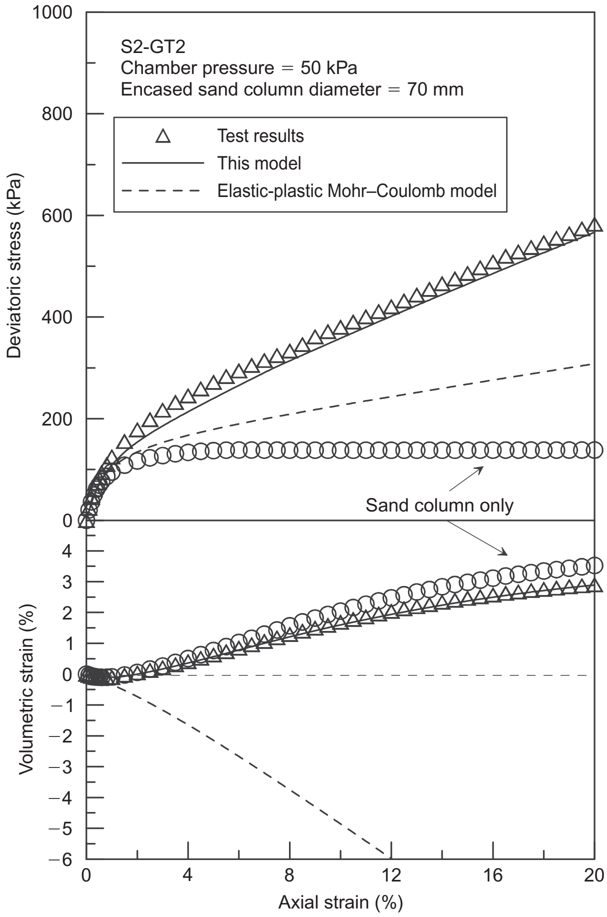

Figure 11. Triaxial compression test results for sand S2 encased by geotextile GT2

The solid lines in Figure 12 show the numerically calculated deviatoric stresses and volumetric strains for encased sand columns in laboratory tests. This figure reveals very good agreements in both deviatoric stress and volumetric strain between the experimental and calculated values for an S2 sand column encased with GT2 geotextile. The calculated deviatoric stress agrees well with the experimental results for the S1 sand column encased in GT1 geotextile. However, most of the calculated volumetric strain values are higher than the measurement results.

The circumferential tensile stress of the encasement due to column expansion increases the confining pressure. The increase in confining pressure due to encasement stretching is referred to herein as ‘induced confining pressure, σ_f’. Figure 13 shows the calculated induced confining pressure for the S1-GT1 and S2-GT2 soil-encasement columns. This figure reveals that geotextiles with relatively low stiffness (30.51 kN/m and 35.30 kN/m for GT1 and GT2) significantly increase the confining pressure on a small-diameter sand column (70 mm). The variation in volumetric strain against chamber pressure for the S1 sand disperses to a greater range (Figure 1), subsequently leading to the S1-GT1 soil-encasement columns spreading their induced confining pressures to a greater range

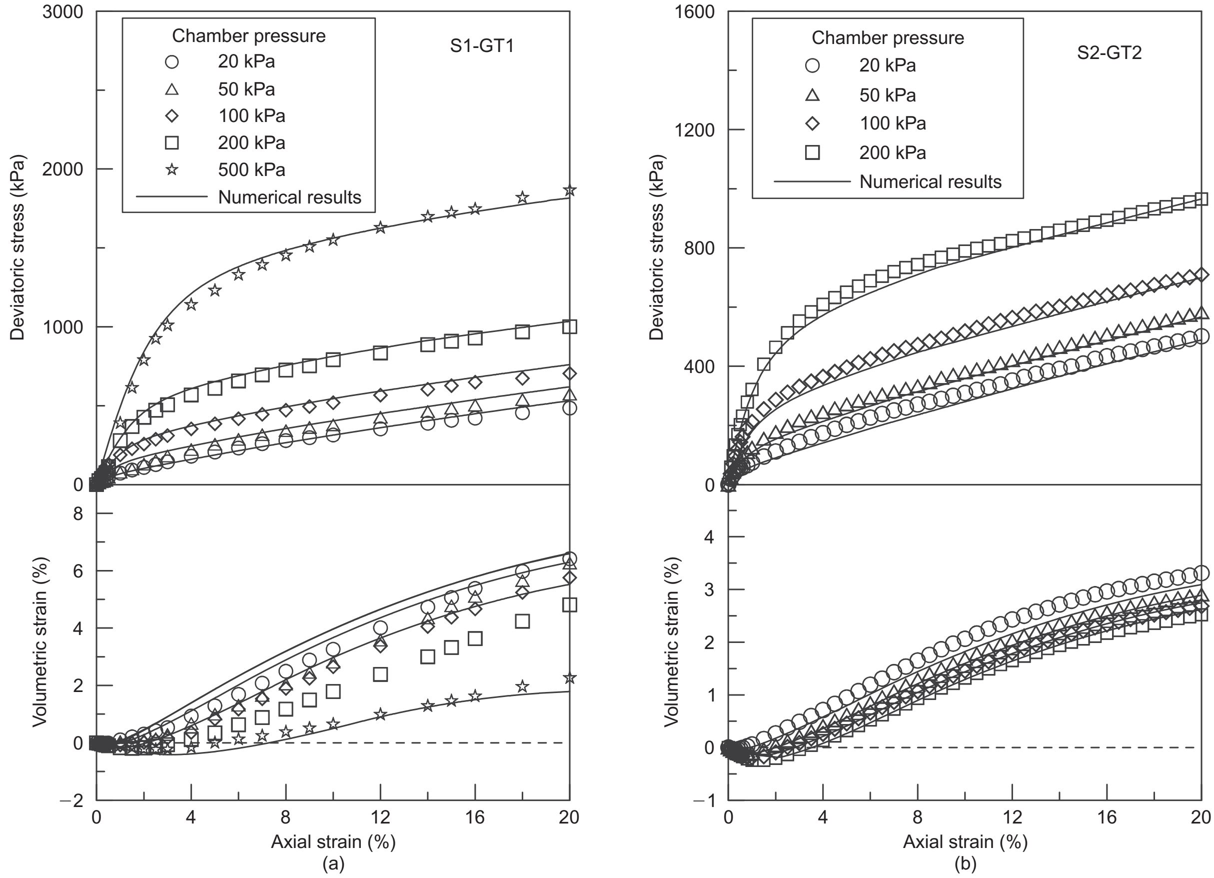

Figure 12. The measured and numerically calculated results for encased sand columns: (a) S1-GT1 sand-encasement column; (b) S2-GT2 sand-encasement column

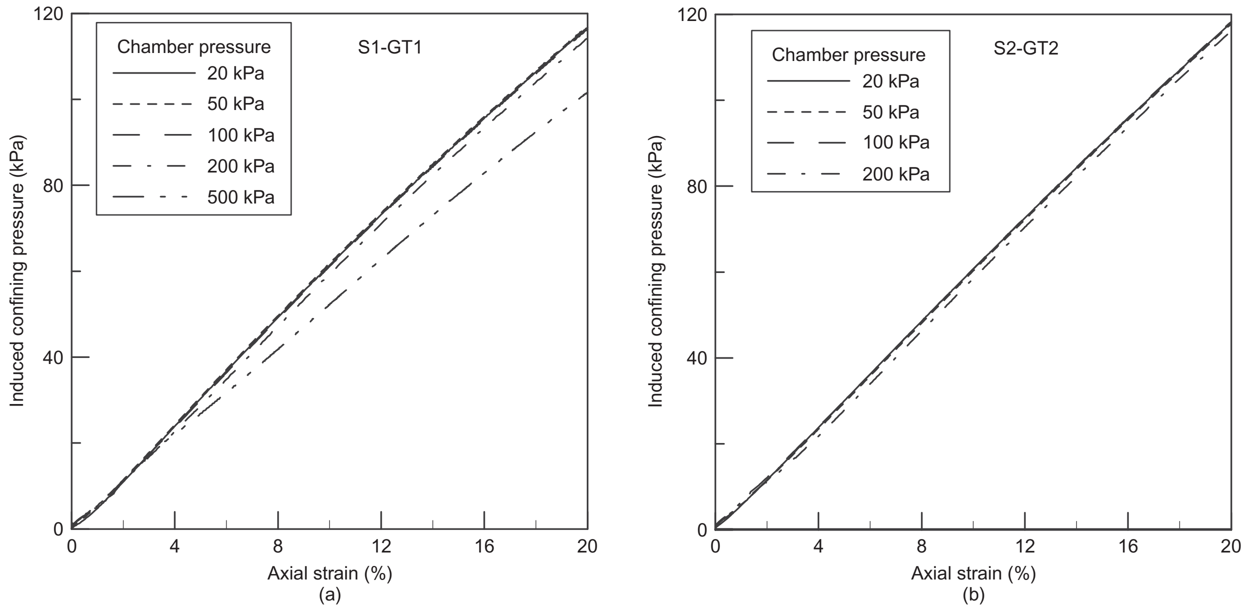

Figure 13. Induced confining pressure by the encasement: (a) S1-GT1 sand-encasement column; (b) S2-GT2 sand-encasement column

(Figure 13a). Conversely, chamber pressure affects, to a lesser extent, the induced confining pressure for the S2-GT2 soil-encasement column (Figure 13b). Analysis results indicate that the volumetric strain of pure sand profoundly affects the induced confining pressure of an encased column. These results also demonstrate the importance of accurate volumetric strain evaluation for pure sand.

3.2. Parametric studies

This section examines the column diameter, and encasement stiffness and strength effects on the encased column performance. This study numerically investigates the behaviour of the encased column using the proposed model.

3.2.1. *Effect of column diameter on encased column response*

Encasement with three elastic moduli (35.3 kN/m, 100 kN/m, 1000 kN/m) is used to encase a column consisting of S2 sand. The columns for each of the three encasement elastic moduli have diameters 70 mm, 200 mm, 500 mm, 750 mm and 1000 mm. In the analyses, the encasement is assumed here to extend without yielding in strength.

Figure 14 displays the variations in deviatoric stress and volumetric strain against axial strain for columns of various diameters. Figure 14a indicates that an encasement with low stiffness can significantly affect the deviatoric stress for a small (70 mm) diameter column. However, the reinforcing effect decreases with increasing column diameter. Also, a low-stiffness encasement slightly affects the deviatoric stress for a large-diameter column (1000 mm). Obviously, an encasement with high stiffness markedly affects columns of all sizes. However, using a high-stiffness encasement to reinforce a small-diameter column dramatically increases the column strength (Figure 14c).

3.2.2. *Effect of encasement stiffness on encased column response*

The extent to which encasement stiffness affects a 0.5 m diameter column composed of S2 sand is examined using the proposed numerical model. The encased column sustains a chamber pressure of 50 kPa. The encasement stiffness J ranges from 35.3 kN/m to 5000 kN/m, which includes various encasement materials. Figure 15 summarises the numerical results. Again, the encasement is assumed here to extend without yielding in strength.

Figure 15 displays the values of deviatoric stress and induced confining pressure at 20% axial strain corresponding to different stiffnesses of encasement. As is expected, the higher the encasement stiffness the higher the deviatoric stress and induced confining pressure, and the lower the volumetric strain. From this, a high-stiffness encasement restrains the development of volumetric strain more (Figure 15a); a column encased with a higher-stiffness encasement generates a lower efficiency in confining pressure increment. The ratio σ_f/J (unit: 1/m) of an encased column at 20% axial strain decreases from 0.482 to 0.415 for encasement stiffness ranging from 35.3 kN/m to 5000 kN/m.

Figure 15 reveals that different encasement stiffnesses and column diameters comprise encased columns with the same stiffness/diameter ratio and produce the same results ($J = 500$ kN/m, $D = 0.5$ m; and $J = 1000$ kN/m, $D = 1.0$ m).

The circumferential (ring) tensile strain of the encasement can be calculated using Equation 25 (Wu and Hong 2009).

$$\varepsilon_\theta = \frac{r_1 - r_0}{r_0} = \sqrt{\frac{1-\varepsilon_v}{1-\varepsilon_1}} - 1 \tag{25}$$

Additionally, the reinforcing effect of an encasement can be represented in terms of induced confining pressure. By assuming a constant encasement stiffness, the encasement-induced confining pressure σ_f can be expressed as

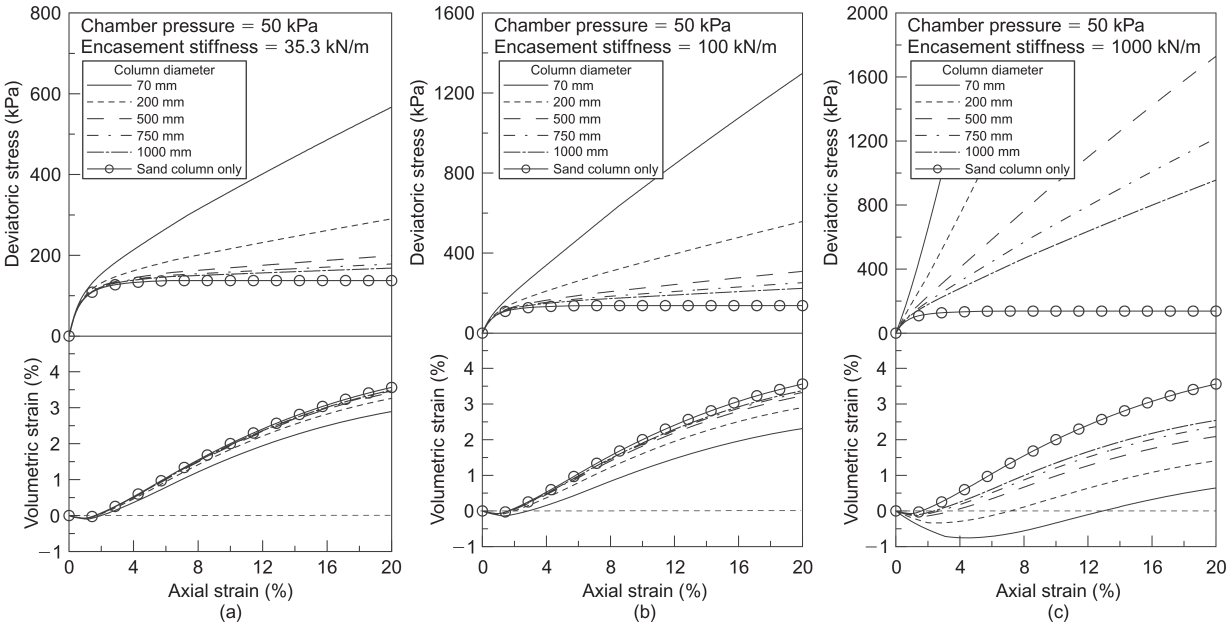

Figure 14. The effect of column diameter on encased column behaviour: (a) encasement stiffness = 35.3 kN/m; (b) encasement stiffness = 100 kN/m; (c) encasement stiffness = 1000 kN/m

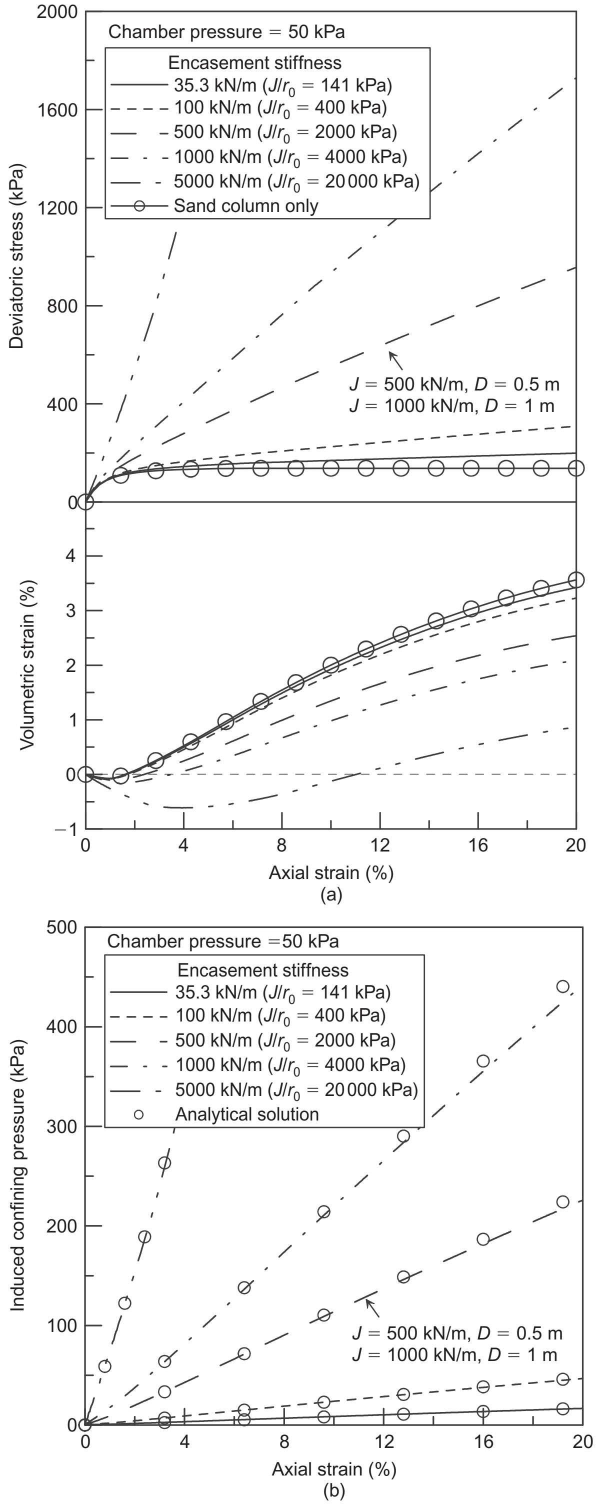

Figure 15. The effect of encasement stiffness on encased column behaviour: (a) deviatoric stress–volumetric strain–axial strain; (b) induced confining pressure

$$\sigma_{\mathrm{f}} = \frac{J\varepsilon_\theta}{r_1} = \frac{J}{r_0}\left[1 - \frac{1}{\sqrt{\dfrac{1-\varepsilon_{\mathrm{v}}}{1-\varepsilon_1}}}\right] \tag{26}$$

Figure 15b plots the encasement-induced confining pressures evaluated using Equation 26. The agreement between numerical analysed and closed form solutions was satisfactory.

3.2.3. *Effect of encasement strength on encased column response*

For an encased column, the increased confining pressure mobilises the compressive strength and resistance to further deformation of the column in an interactive manner. Therefore, no distinct sign of strength yield can be found in the encased columns, especially for a small-diameter column or a column encased with a high-stiffness encasement material (Figures 14 and 15a).

The above inference can be drawn only on the basis of no yield in the encasement strength assumption. Next, exactly how the encasement strength affects the performance of an encased column is illustrated using a 0.5 m diameter column. The column sustained 50 kPa chamber pressure and was encased with encasements of two stiffness (100 kN/m and 1000 kN/m). Figure 16 describes the deviatoric stress and volumetric strain for column encased with encasements of various strengths. A distinct encased-column yield due to encasement yielding is observed.

If the encasement yield strain $\varepsilon_{\mathrm{y}} = T_{\mathrm{fy}}/J$, where T_{fy} denotes the tensile strength of the encasement, exceeds the circumferential strain ε_θ calculated using Equation 25 (i.e. $\varepsilon_{\mathrm{y}} \geqslant \varepsilon_\theta$), the encased column does not yield prior to the axial strain ε_1.

For a column wrapped with encasement of $J = 1000$ kN/m and $T_{\mathrm{fy}} = 10$ kN/m, 50 kN/m and 100 kN/m, the axial strains corresponding to the yield of the encased columns are 2.1%, 9.2% and 18.1%, respectively (Figure 16a). The yield of an encased column with $J = 100$ kN/m and $T_{\mathrm{fy}} = 10$ kN/m occurs at an axial strain of 17.1% (Figure 16b).

4. CONCLUSIONS

This study presented a numerical analysis method to elucidate the behaviour of geosynthetic-encased sand columns. An important characteristic, the dilative behaviour, of the medium to dense sand was also examined. This study investigated the behaviour of a single reinforced column subjected to constant external confining pressure. Although the studied column and columns embedded in the field differ somewhat in load and boundary conditions, understanding the reinforcing mechanism and the factors essential to the column behaviour contributes significantly to advancement of embedded column studies. The following conclusions can be drawn from the results of this study.

- The simple elastic-plastic model with Mohr–Coulomb yield criterion accurately predicts deviatoric stress for pure soil. However, the simple model underestimates the deviatoric stress for the encased column due to the inability to evaluate the volumetric strain of sand in the pre-yield state. Generally, the simple model predicts volume contraction until the yield state, which contradicts the volumetric expansion behaviour for most medium to dense sands and ultimately underestimates the induced confining pressure.

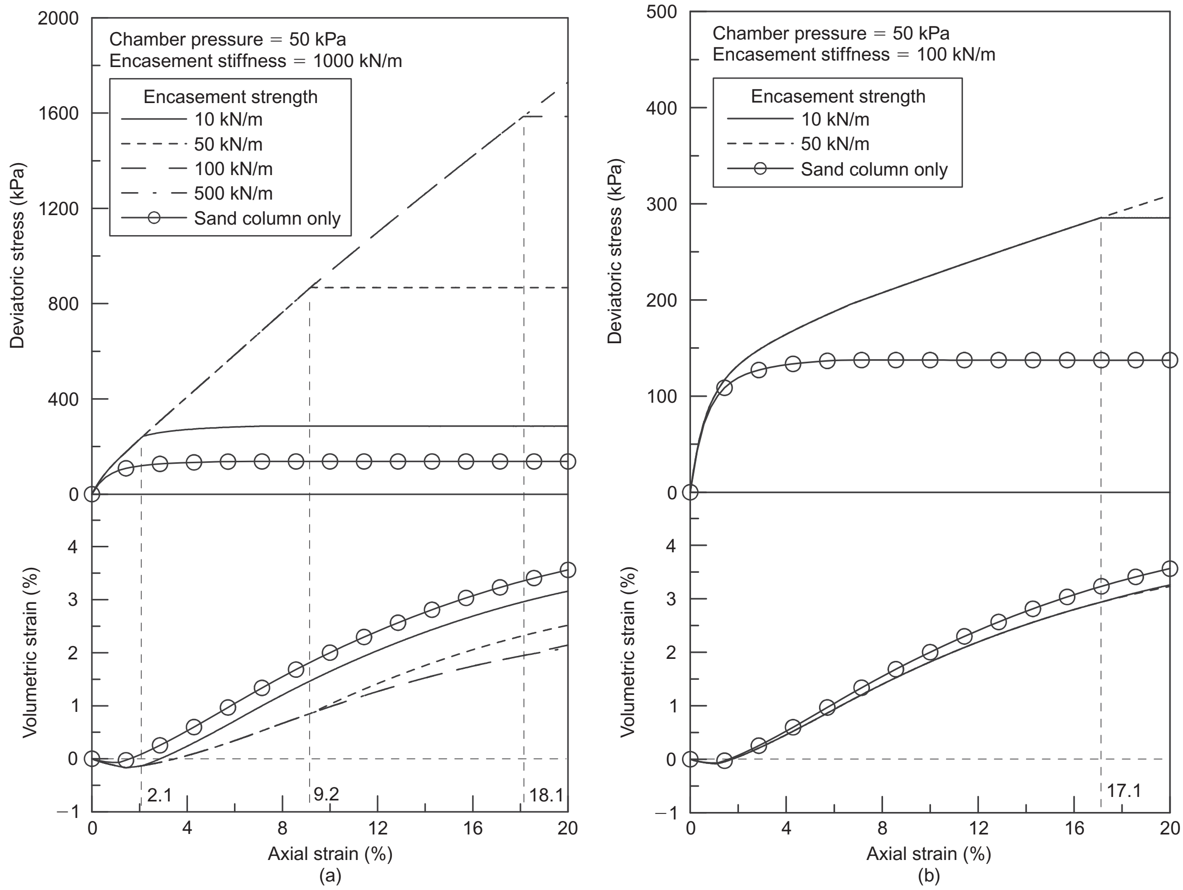

Figure 16. The effect of encasement strength on encased column behaviour: (a) encasement stiffness = 1000 kN/m; (b) encasement stiffness = 100 kN/m

- Results obtained from the proposed numerical model correspond closely to the laboratory-observed results for un-reinforced and encased columns, both in deviatoric stress and volumetric strain. Thorough elucidation of the volumetric strain behaviour of the filled material is essential for accurately predicting encased column performance.
- For a sand column encased by a tensile resistant sleeve, the chamber pressure only slightly affects the magnitude of the induced confining pressure if the volumetric strain with chamber pressure for the pure sand varies only slightly. The two encased sand columns tested have a small range in induced confining pressure for chamber pressure ranging from 20 kPa to 200 kPa.
- The encasement stiffness and column diameter significantly affect the induced confining pressure of an encased column. Numerical results indicate that using a low-stiffness encasement to reinforce a large-diameter column produces a limited reinforcement effect. However, using a high-stiffness encasement to reinforce a small-diameter column results in an excessively high confining pressure.
- The sleeve hoop stress exerts an additional confining pressure on the encased column, subsequently mobilising its compressive strength and resistance to further deformation in an interactive manner. Therefore, no distinct sign of strength yield can be found in the encased columns before the encasement reaches its yield strength.

ACKNOWLEDGEMENTS

The author would like to thank the National Science Council of the Republic of China for financially supporting this research under Contract no. NSC99–2221-E-032–046-MY2. The value of discussion with C-S. Wu at Tamkang University is greatly appreciated. The contribution of C. J. Wei in the laboratory tests is gratefully acknowledged.

NOTATION

Basic SI units are given in parentheses.

B	bulk modulus (Pa)
c	cohesion (Pa)
$d\varepsilon_{ij}^{\mathrm{p}}$	plastic strain increment (dimensionless)
$d\varepsilon_{\mathrm{v}}^{\mathrm{p}}$	volumetric plastic strain increment (dimensionless)
$d\varepsilon_{1}^{\mathrm{p}}$	plastic strain increment in the axial direction (dimensionless)
$d\varepsilon_{3}^{\mathrm{p}}$	plastic strain increment in the radial directions (dimensionless)
D	diameter of column (m)

E elastic modulus (Pa)
f yield function (Pa)
g plastic potential function (Pa)
G_s specific gravity of soil solids (dimensionless)
J stiffness of encasement (N/m)
N_{ϕ^*} mobilised friction angle function (dimensionless)
N_{ψ^*} mobilised dilatancy angle function (dimensionless)
P_a atmospheric pressure (Pa)
r_0 initial radii of column (m)
r_1 deformed radii of column (m)
T_{fy} tensile strength of the encasement (N/m)
u unit step function (dimensionless)
ϕ^* mobilised friction angle (degrees)
$\gamma_{d\max}$ maximum dry unit weight (N/m^3)
$\gamma_{d\min}$ minimum dry unit weight (N/m^3)
ε_a axial strain (dimensionless)
ε_a^e axial elastic strain (dimensionless)
ε_a^p accumulated axial plastic strain (dimensionless)
ε_r^p accumulated radial plastic strain (dimensionless)
ε_{rad} radial strain of column (dimensionless)
ε_s^p accumulated shear plastic strain (dimensionless)
$\varepsilon_{s,exp}^p$ accumulated shear plastic strain at initial dilation (dimensionless)
$\varepsilon_{s,peak}^p$ accumulated shear plastic strain at the peak deviatoric stress (dimensionless)
$\varepsilon_{s,res}^p$ accumulated shear plastic strain at the peak mobilised dilatancy angle, or the initial residual stage (dimensionless)
ε_v volumetric strain (dimensionless)
ε_v^p accumulated volumetric plastic strain (dimensionless)
ε_v^e volumetric elastic strain (dimensionless)
ε_y encasement yield strain (dimensionless)
ε_1 axial strain (dimensionless)
ε_θ encasement circumferential strain (dimensionless)
λ positive scale value (dimensionless)
σ_f induced confining pressure (Pa)
$\boldsymbol{\sigma}_{ij}$ stress tensor (Pa)
σ_1 major principal stress (Pa)
σ_3 minor principal stress (Pa)
ψ^* mobilised dilatancy angle (degrees)
$\Delta\sigma$ deviatoric stress (Pa)

REFERENCES

Alamgir, M., Miura, N., Poorooshasb, H. B. & Madhav, M. R. (1996). Deformation analysis of soft ground reinforced by columnar inclusions. *Computers and Geotechnics*, **18**, No. 4, 267–290.

Alexiew, D., Brokemper, D. & Lothspeich, S. (2005). Geotextile encased columns (GEC): load capacity, geotextile selection and pre-design graphs. *Proceedings of the Geo-Frontiers Conference*, Austin, TX, USA, ASCE Geotechnical Special Publication No. 131, ASCE, Reston, VA, USA, pp. 497–510.

Ali, K., Shahu, J. T. & Sharma, K. G. (2012). Model tests on geosynthetic-reinforced stone columns: a comparative study. *Geosynthetics International*, **19**, No. 4, 292–305.

Ambily, A. P. & Gandhi, S. R. (2007). Behavior of stone columns based on experimental and FEM analysis. *ASCE Journal of Geotechnical and Geoenvironmental Engineering*, **133**, No. 4, 405–415.

Araujo, G. L. S., Palmeira, E. M. & Cunha, R. P. (2009). Behaviour of geosynthetic-encased granular columns in porous collapsible soil. *Geosynthetics International*, **16**, No. 6, 433–451.

Ayadat, T. & Hanna, A. M. (2005). Encapsulated stone columns as a soil improvement technique for collapsible soil. *Proceedings of the Institution of Civil Engineers – Ground Improvement*, **9**, No. 4, 137–147.

Broms, B. B. (1977). Triaxial tests with fabric-reinforced soil. *Proceedings of the International Conference on the Use of Fabric in Geotechnics*, Ecole Nationale des Ponts et Chaussees, Paris, France, Vol. 3, pp. 129–134.

Broms, B. B. (1995). Fabric reinforced soil. *Developments in Deep Foundations and Ground Improvement Schemes*. Balasubramaniam, A. S., Bergado, D. T., Phien-Wej, N., Hong, S. W., Ashford, S. A. & Nutalaya, P., Editors, Balkema, Rotterdam, Netherlands, pp. 261–291.

Canetta, G. & Nova, R. (1989). Numerical method for the analysis of ground improved by columnar inclusions. *Computers and Geotechnics*, **7**, No. 1–2, 99–114.

Chandrasekaran, B., Broms, B. & Wong, K. S. (1989). Strength of fabric reinforced sand under axisymmetric loading. *Geotextiles and Geomembranes*, **8**, No. 4, 293–310.

de Mello, L. G., Mondolfo, M., Montez, F., Tsukahara, C. N. & Bilfinger, W. (2008). First use of geosynthetic encased sand columns in South America. *Proceedings of 1st Pan-American Geosynthetics Conference*, Cancún, Mexico, pp. 1332–1341.

Gniel, J. & Bouazza, A. (2009). Improvement of soft soils using geogrid encased stone columns. *Geotextiles and Geomembranes*, **27**, No. 3, 167–175.

Gray, D. H. & Al-Refai, T. (1986). Behavior of fabric vs. fiber-reinforced sand. *ASCE Journal of Geotechnical Engineering Division*, **112**, No. 8, 804–820.

Han, J. & Gabr, M. A. (2002). Numerical analysis of geosynthetic-reinforced and pile-supported earth platforms over soft soil. *ASCE Journal of Geotechnical and Geoenvironmental Engineering*, **128**, No. 1, 44–53.

Huang, B., Bathurst, R. J. & Hatami, K. (2009). Numerical study of reinforced soil segmental walls using three different constitutive soil models. *ASCE Journal of Geotechnical and Geoenvironmental Engineering*, **135**, No. 10, 1486–1498.

Hughes, J. M. O. & Withers, N. J. (1974). Reinforcing of soft cohesive soils with stone columns. *Ground Engineering*, **7**, No. 3, 42–49.

Hughes, J. M. O., Withers, N. J. & Greenwood, D. A. (1975). A field trial of the reinforcing effect of a stone column in soil. *Géotechnique*, **25**, No. 1, 31–44.

Kempfert, H. G., Jaup, A. & Raithel, M. (1997). Interactive behaviour of a flexible reinforced sand column foundation in soft soils. *Proceedings of 14th International Conference on Soil Mechanics and Geotechnical Engineering*, Hamburg, Germany, pp. 1757–1760.

Kempfert, H. G. (2003). Ground improvement methods with special emphasis on column-type techniques. *International Workshop on Geotechnics of Soft Soils – Theory and Practice*, Vermeer, P. A., Schweiger, H. F., Karstunen, M. & Cudny, M., Editors, Glückauf Verlag, Essen, Germany, pp. 101–112.

Khabbazian, M., Kaliakin, V. N. & Meehan, C. L. (2010). Numerical study of the effect of geosynthetic encasement on the behaviour of granular columns. *Geosynthetics International*, **17**, No. 3, 132–143.

Lee, J. S. & Pande, G. N. (1998). Analysis of stone-column reinforced foundations. *International Journal for Numerical and Analytical Methods in Geomechanics*, **22**, No. 12, 1001–1020.

Lo, S. R., Zhang, R. & Mak, J. (2010). Geosynthetic-encased stone columns in soft clay: a numerical study. *Geotextiles and Geomembranes*, **28**, No. 3, 292–302.

Madhav, M. R. & Miura, N. (1994). Soil improvement. Panel report on stone columns. *Proceedings of the 13th International Conference on*

Soil Mechanics and Foundation Engineering, New Delhi, India, Vol. 5, pp. 163–164.

Madhavi, L. & Murthy, V. S. (2007). Effects of reinforcement form on the behavior of geosynthetic reinforced sand. *Geotextiles and Geomembranes*, **25**, No. 1, 23–32.

Malarvizhi, S. N. & Ilamparuthi, K. (2007). Comparative study on the behavior of encased stone column and conventional stone column. *Soils and Foundations*, **47**, No. 5, 873–885.

Miura, S. & Toki, S. (1982). A sample preparation method and its effect on static and cyclic deformation–strength properties of sand. *Soils and Foundations*, **22**, No. 1, 61–77.

Murugesan, S. & Rajagopal, K. (2006). Geosynthetic-encased stone columns: numerical evaluation. *Geotextiles and Geomembranes*, **24**, No. 6, 349–358.

Murugesan, S. & Rajagopal, K. (2007). Model tests on geosynthetic-encased stone columns. *Geosynthetics International*, **14**, No. 6, 346–354.

Murugesan, S. & Rajagopal, K. (2010). Studies on the behavior of single and group of geosynthetic encased stone columns. *ASCE Journal of Geotechnical and Geoenvironmental Engineering*, **136**, No. 1, 129–139.

Nods, M. (2002). Put a sock in it: geotextile enhanced sand columns are preventing settlement of a high-speed railway embankment in the Netherlands. *Ground Engineering*, **35**, No. 12, 25.

Pulko, B., Majes, B. & Logar, J. (2011). Geosynthetic-encased stone columns: analytical calculation model. *Geotextiles and Geomembranes*, **29**, No. 1, 29–39.

Raithel, M. & Kempfert, H. G. (2000). Calculation models for dam foundations with geotextile coated sand columns. *Proceedings of the International Conference on Geotechnical and Geological Engineering, GeoEngg-2000*, Melbourne, Australia, pp. 347.

Raithel, M., Kempfert, H. G. & Kirchner, A. (2002). Geotextile-encased columns (GEC) for foundation of a dike on very soft soils. *Proceedings of the Seventh International Conference on Geosynthetics*, A. A. Balkema, Nice, France, pp. 1025–1028.

Raithel, M., Kirchner, A., Schade, C. & Leusink, E. (2005). Foundation of construction on very soft soils with geotextile encased columns – state of the art. *Proceedings of Geo-Frontiers 2005*, Austin, TX, USA, pp. 1–11.

Rajagopal, K., Krishnaswamy, N. R. & Madhavi Latha, G. (1999). Behaviour of sand confined with single and multiple geocells. *Geotextiles and Geomembranes*, **17**, No. 3, 171–184.

Shahu, J. T., Madhav, M. R. & Hayashi, S. (2000). Analysis of soft ground–granular pile–granular mat system. *Computers and Geotechnics*, **27**, No. 1, 45–62.

Sivakumar Babu, G. L., Vasudevan, A. K. & Haldar, S. (2008). Numerical simulation of fiber-reinforced sand behavior. *Geotextiles and Geomembranes*, **26**, No. 2, 181–188.

Wu, C. S. & Hong, Y. S. (2009). Laboratory tests on geosynthetic-encapsulated sand columns. *Geotextiles and Geomembranes*, **27**, No. 2, 107–120.

Wu, C. S., Hong, Y. S. & Lin, H. C. (2009). Axial stress-strain relation of encapsulated granular column. *Computers and Geotechnics*, **36**, No. 1–2, 226–240.

Yoo, C. & Kim, S. B. (2009). Numerical modeling of geosynthetic-encased stone column-reinforced ground. *Geosynthetics International*, **16**, No. 3, 116–126.

Yoo, C. (2010). Performance of geosynthetic-encased stone columns in embankment construction: numerical investigation. *ASCE Journal of Geotechnical and Geoenvironmental Engineering*, **136**, No. 8, 1148–1160.

Zhang, Y., Li, T. & Wang, Y. (2011). Theoretical elastic solutions for foundations improved by geosynthetic-encased columns. *Geosynthetics International*, **18**, No. 1, 12–20.

The Editor welcomes discussion on all papers published in Geosynthetics International. Please email your contribution to discussion@geosynthetics-international.com by 15 June 2013.